Check for updates

RESEARCH ARTICLE

ADVANCED FUNCTIONAL MATERIALS
www.afm-journal.de

High-Efficiency Electrochemical Nitrogen Fixation by Noble-Metal-Free Metallic Glasses

Xue Chen, Xin-Jie Peng, Dong-Dong Xiao, Yi-Tao Sun, Kai-Ling Zhou, Xiao-Yong Yang, Yong-Zheng Zhang, Wei-Hua Wang, Zhen Lu,* and Hai-Yang Bai**

The electrocatalytic nitrogen reduction reaction (NRR) represents an energy-efficient alternative to the traditional Haber-Bosch process for industrial ammonia synthesis. However, the cleavage of the strong N≡N bond hinders the practical application of NRR. Herein, an innovative design strategy is proposed based on a $Fe_{76}Si_8B_{13}Nb_3$ metallic glass (MG-FeSiBNb) catalyst, featuring a unique amorphous structure with endogenous nanoscale compositional heterogeneity. This catalyst achieves an impressive ammonia yield rate of 92.1 µg h^{-1} $mg^{-1}_{cat.}$ in 0.1 м Na_2SO_4 solution, surpassing most state-of-the-art NRR electrocatalysts. Extended X-ray absorption fine structure analysis reveals that MG-FeSiBNb provides abundant unsaturated coordination sites, essential for effective N_2 adsorption. Furthermore, electronic structural characterizations and density functional theory calculations demonstrate that the incorporation of Si, B, and Nb atoms into the Fe-based matrix precisely tailors the local electronic environment, effectively shifting the Fe d-band center toward the Fermi level. This electronic modulation enhances electron transfer efficiency, thus promoting the hydrogenation of $^*NH_2$ to $^*NH_3$. Additionally, the amorphous nature of MG-FeSiBNb suppresses hydrogen adsorption by eliminating well-defined crystal facets, thereby selectively mitigating the hydrogen evolution reaction and enhancing NRR selectivity. This work offers not only a high-performing NRR catalyst but also a generalizable strategy for sustainable electrocatalysis beyond conventional crystalline systems.

1. Introduction

As a critical precursor for fertilizer and a promising carbon-free energy carrier with high hydrogen density, the artificial fixation of nitrogen (N_2) to ammonia (NH_3) is indispensable in both agriculture and industry.[1–5] This process utilizes the abundance of atmospheric N_2 but faces significant challenges due to the extremely high bond energy (941 kJ mol^{-1}) and the absence of a permanent dipole in the N≡N triple bond, which makes activation highly demanding.[6–9] Despite being established over a century ago, the Haber-Bosch process remains the predominant industrial method for NH_3 synthesis, it operates under harsh conditions (temperatures of 300 to 500 °C, and pressures of 150 to 300 atm) with substantial energy consumption (>600 kJ mol^{-1}).[10–13] As a more sustainable alternative, the electrochemical nitrogen reduction reaction (NRR) enables the conversion of atmospheric N_2 and water to NH_3 under ambient conditions,[12,14,15] which has attracted tremendous attention for its potential to reduce the energy and environmental impact associated with the

X.-J. Peng, D.-D. Xiao, Y.-T. Sun, W.-H. Wang, Z. Lu, H.-Y. Bai
Institute of Physics
Chinese Academy of Sciences
Beijing 100190, China
E-mail: zhenlu@iphy.ac.cn; hybai@iphy.ac.cn

X. Chen, X.-Y. Yang, Y.-Z. Zhang
School of Physics and Physical Engineering
Qufu Normal University
Qufu 273165, China
E-mail: yzzhang@qfnu.edu.cn

K.-L. Zhou
The Key Laboratory of Advanced Functional Materials
Ministry of Education of China
Faculty of Materials and Manufacturing
Beijing University of Technology
Beijing 100124, China

Z. Lu
School of Physical Sciences
University of Chinese Academy of Sciences
Beijing 100049, China

W.-H. Wang
Songshan Lake Materials Laboratory
Dongguan, Guangdong 523808, China

H.-Y. Bai
Center of Materials Science and Optoelectronics Engineering
University of Chinese Academy of Sciences
Beijing 100049, China

The ORCID identification number(s) for the author(s) of this article can be found under https://doi.org/10.1002/adfm.202503400

DOI: 10.1002/adfm.202503400

© 2025 Wiley-VCH GmbH

16163028, 0, Downloaded from https://advanced.onlinelibrary.wiley.com/doi/10.1002/adfm.202503400 by Institute Of Physics Chinese Academy Of Sciences, Wiley Online Library on [12/08/2025]. See the Terms and Conditions (https://onlinelibrary.wiley.com/terms-and-conditions) on Wiley Online Library for rules of use; OA articles are governed by the applicable Creative Commons License

Haber-Bosch process.[16–19] Noble metal electrocatalysts are acknowledged for their remarkable NRR performance, attributed to their optimal N_2 adsorption capacities, high density of active sites, and exceptional electrical conductivities.[20,21] However, their widespread industrial application is hindered by high costs, complex synthesis procedures, and limited long-term stability.[22,23] In contrast, non-noble transition metal-based materials offer a promising alternative. With their abundant d-orbital electrons and unoccupied orbitals, these materials effectively activate the robust N≡N triple bond, making them attractive candidates for NRR catalysis.[24,25] Nonetheless, despite considerable advancements in designing efficient NRR catalysts, many electrocatalysts suffer from low NH_3. This limitation arises from excessively strong binding to N_2 species, which slows the slow desorption of certain intermediates and inhibits overall reaction efficiency.[26,27]

Metallic glasses (MGs), characterized by their disordered atomic packing structure, are metastable materials that exist in a state far from equilibrium compared to their crystalline counterparts.[28–30] These materials exhibit exceptional mechanical and chemical properties, including high strength, robust corrosion resistance, and enhanced surface reactivity.[31–34] Their unique characteristics, such as a significant number of low-coordination surface atoms and highly tunable compositions, position MGs as promising candidates for catalytic applications.[35–41] Among them, Fe-based MGs stand out due to their cost-effective production, environmental friendliness, straightforward synthesis, and excellent reducibility, making them highly suitable for applications such as oxygen evolution reaction, wastewater remediation, and energy conversion.[32,42,43] However, research on Fe-based MG catalysts for NRR remains scarce. Furthermore, most reported NRR catalysts suffer from low active site density, insufficient N_2 adsorption strength, or strong competition from the hydrogen evolution reaction (HER). By leveraging the disordered structure of MGs, it becomes possible to overcome these limitations. The lack of long-range periodicity in MGs enables continuous modulation of the local electronic structure, facilitating the formation of active sites with tailored adsorption properties for N_2 molecules. More importantly, the inherent flexibility in compositional design allows for the strategic incorporation of elements to further regulate the d-band center of the active metal, enhancing both selectivity and efficiency. Thus, exploring and optimizing Fe-based MG catalysts with high NH_3 yield rate is pivotal for advancing the development of innovative noble-metal-free NRR catalysts.

In this work, we synthesized a noble-metal-free $Fe_{76}Si_8B_{13}Nb_3$ (FeSiBNb) MG film featuring nanoscale phase separation through a straightforward ion-beam deposition (IBD) method utilizing a rapid surface diffusion mechanism, which introduces interfacial heterogeneity and enhances surface complexity. Remarkably, this FeSiBNb MG film achieves an exceptionally high NH_3 yield of 92.1 μg h^{-1} $mg^{-1}{}_{cat.}$ at −0.8 V versus the reversible hydrogen electrode (RHE) under ambient temperature and pressure conditions, which surpasses the performance of most NRR electrocatalysts. The enhanced electrocatalytic activity of the FeSiBNb MG film is attributed to its abundance of unsaturated coordination sites, facilitating the adsorption of N_2. The introduction of Nb promotes phase separation, which exhibits reduced charge transfer resistance and facilitates charge transfer. Additionally, electronic structural characterizations and theoretical simulations reveal that the incorporation of Si, B, and Nb modifies the local electronic environment of Fe atoms, increasing the availability of electronically active Fe d-state, enhancing both the adsorption strength and the catalytic activity toward NRR. This modification facilitates the rate-determining step of hydrogenating adsorbed $^*NH_2$ intermediates to $^*NH_3$ through enhanced electron transfer. This synergistic elemental engineering provides a new direction in tailoring MG catalysts for NRR.

2. Results and Discussion

2.1. Catalyst Syntheses and Structural Characterizations

$Fe_{76}Si_8B_{13}Nb_3$ (atomic ratio) MG films were fabricated using the IBD method at a constant deposition rate of 3 nm min^{-1}, resulting in a film thickness of 2 μm (denoted as MG-FeSiBNb). Figure S1a (Supporting Information) shows the differential scanning calorimetry (DSC) profile of MG-FeSiBNb, displaying clear glass transition and crystallization signals, confirming its glassy nature. The crystallized counterpart (referred to as C-FeSiBNb) was achieved by fully annealing the sample at 900 °C (above the crystallization temperature, T_x) for 60 min in a high vacuum environment (better than 1.0×10^{-4} Pa) to prevent surface oxidation that could potentially affect its catalytic properties. In contrast to MG-FeSiBNb, C-FeSiBNb exhibits distinct crystallization peaks corresponding to α-Fe and Fe_3Si phases (Figure S1b, Supporting Information). $Fe_{76}Si_8B_{13}Nb_3$ MG ribbons, with a thickness of 10 μm and a width of 2 mm, were prepared by melt-spinning under an argon atmosphere (denoted as MG-FeSiBNb ribbon). Further details are available in the Experimental Section (Supporting Information). High-resolution transmission electron microscopy (HRTEM) images and the corresponding selected area electron diffraction (SAED) patterns demonstrate that MG-FeSiBNb exhibits a spinodal decomposition morphology with average sizes of ≈1.4 ± 0.5 nm and 4.7 ± 1.5 nm (**Figure 1a**). In contrast, C-FeSiBNb features distinct nanocrystalline phases with an average size distribution of 13.5 ± 2.6 nm (Figure 1b). Additionally, the MG-FeSiBNb ribbon shows a homogeneous amorphous structure without apparent phase separation (Figure S2, Supporting Information).

X-ray absorption near-edge structure (XANES) and extended X-ray absorption fine structure (EXAFS) analyses were conducted to investigate the chemical environments of Fe species at the atomic level in both MG-FeSiBNb and C-FeSiBNb samples. Remarkably, the Fe absorption K-edges in these samples closely resemble those observed in the Fe foil reference, indicating that the Fe species maintain a metallic state with electronic structures similar to that of pure Fe, as shown in Figure 1c. The Fourier transformed EXAFS curves for both samples reveal a prominent peak ≈2 Å, corresponding to Fe-Si and Fe-Fe scattering paths, compared with reference spectra from $FeSi_2$ and Fe foils (Figure 1d). Additionally, the intensity of the main scattering peak in MG-FeSiBNb is lower than that in C-FeSiBNb, suggesting a reduced coordination number and greater disorder in the glassy state (Figure 1d).[44,45] Least-squares curve parameter fitting was performed to quantitatively determine structural parameters of Fe species in both MG-FeSiBNb and C-FeSiBNb (Figures S3, S4 and Text S1 for details, Supporting Information).

© 2025 Wiley-VCH GmbH

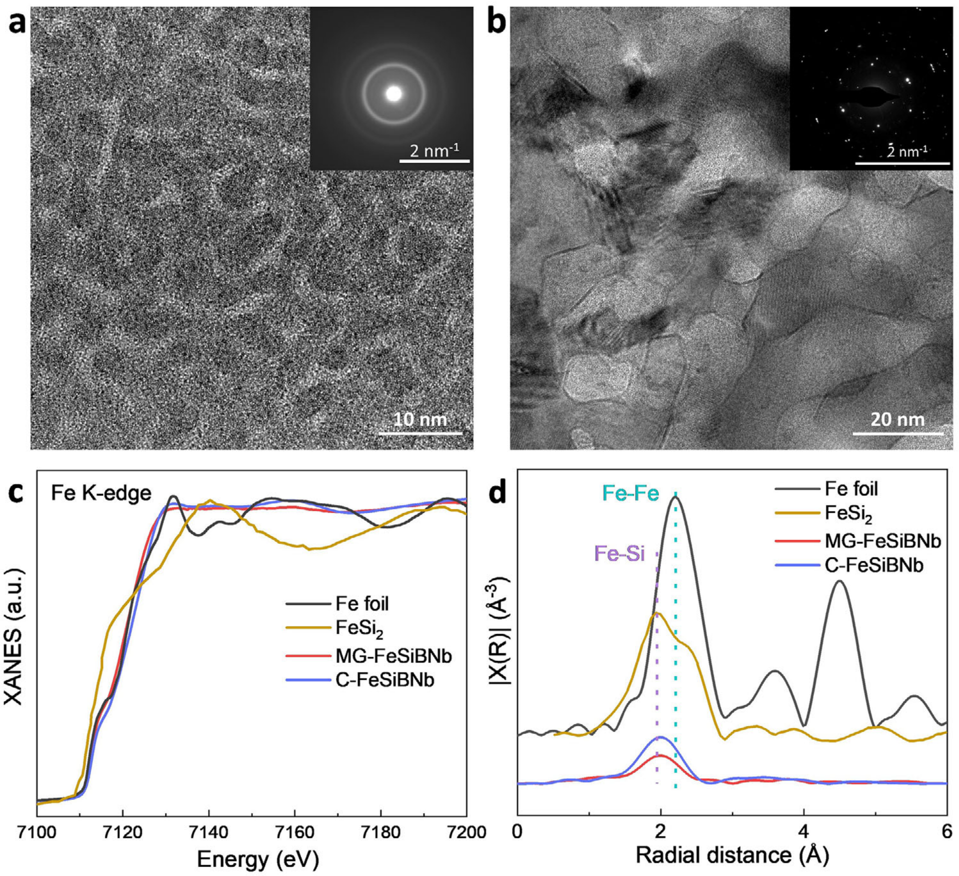

Figure 1. HRTEM images of a) MG-FeSiBNb and b) C-FeSiBNb. The insets present the corresponding selected electron diffraction (SAED) patterns. c) Fe K-edge XANES spectra of MG-FeSiBNb, Fe foil, $FeSi_2$, and C-FeSiBNb. d) Fourier transform EXAFS spectra of MG-FeSiBNb in reference to Fe foil, $FeSi_2$, and C-FeSiBNb.

In the glassy state, MG-FeSiBNb presents reduced coordination numbers for Fe-Si and Fe-Fe at the first neighbor shell (Table S1, Supporting Information), indicating the presence of numerous under-saturated coordination sites. Moreover, the corresponding wavelet transform image of MG-FeSiBNb demonstrates a rightward shift in the coordination bond/intensity maximum, suggesting that Fe species preferentially bond with heavier elements in the glassy state (Figure S5, Supporting Information).

The elemental chemical states of MG-FeSiBNb, C-FeSiBNb, and MG-FeSiBNb ribbon were elucidated by X-ray photoelectron spectroscopy (XPS). Gaussian fitting was employed to deconvolute the Fe 2p, Si 2p, B 1s, and Nb 3d spectra, providing a comprehensive understanding of the chemical environments in these samples, as illustrated in **Figure** 2a,b Figure S6 (Supporting Information). The high-resolution Fe 2p spectra for the samples display three spin–orbit bimodal peaks along with two vibrating satellites (Figure 2a). For MG-FeSiBNb, binding energies at 707.0 and 719.9 eV are indicative of Fe^0.[46] Furthermore, Fe 2p XPS spectra also reveal the presence of oxidized Fe species. Additionally, satellite peaks associated with Fe 2p appear at binding energies of 715.8 and 730.3 eV. Comparatively, the Fe 2p spectrum of C-FeSiBNb demonstrates a slight shift of 0.3 eV toward higher binding energies. The Fe 2p peaks of the MG-FeSiBNb ribbon exhibit minimal deviation from those of the MG-FeSiBNb. Furthermore, the binding energies for Si 2p and B 1s in MG-FeSiBNb are lower than those observed in C-FeSiBNb, suggesting differences in their chemical states (Figure 2a,b; Figure S6, Supporting Information). Compared to its crystalline counterpart, MG-FeSiBNb is characterized by a large number of "dangling-bonds" with a reduced coordination number, which are responsible for the observed low energy shifts in the XPS spectra.[30,47] These negative shifts in binding energies lead to electron enrichment on the surface.[48] The unique surface atomic configuration and electron distribution in MG-FeSiBNb contribute to an expanded number of electrochemically active sites, enhancing the adsorption of N_2-containing intermediates and improving catalytic performance.[49,50]

The process of heterogeneous catalysis begins with the adsorption of reactants onto the surface of the catalyst. Therefore, the adsorption of N_2 and intermediate substances at the active sites of the catalyst is a critical factor in electrocatalytic reactions, closely associated with the valence electron state of the catalyst. The interaction strength between catalysts and adsorbates can be anticipated by analyzing the average energy of the d electrons.[51] Since the NRR mainly involves the interaction between the d orbital of Fe and the p or s orbital of the $^*N_2$ adsorbate, a d-band center closer to the Fermi level typically signifies enhanced adsorption capabilities, which is vital for effective catalysis.[52,53]

16163028, 0, Downloaded from https://advanced.onlinelibrary.wiley.com/doi/10.1002/adfm.202503400 by Institute Of Physics Chinese Academy Of Sciences, Wiley Online Library on [12/08/2025]. See the Terms and Conditions (https://onlinelibrary.wiley.com/terms-and-conditions) on Wiley Online Library for rules of use; OA articles are governed by the applicable Creative Commons License

16163028, 0, Downloaded from https://advanced.onlinelibrary.wiley.com/doi/10.1002/adfm.202503400 by Institute Of Physics Chinese Academy Of Sciences, Wiley Online Library on [12/08/2025]. See the Terms and Conditions (https://onlinelibrary.wiley.com/terms-and-conditions) on Wiley Online Library for rules of use; OA articles are governed by the applicable Creative Commons License

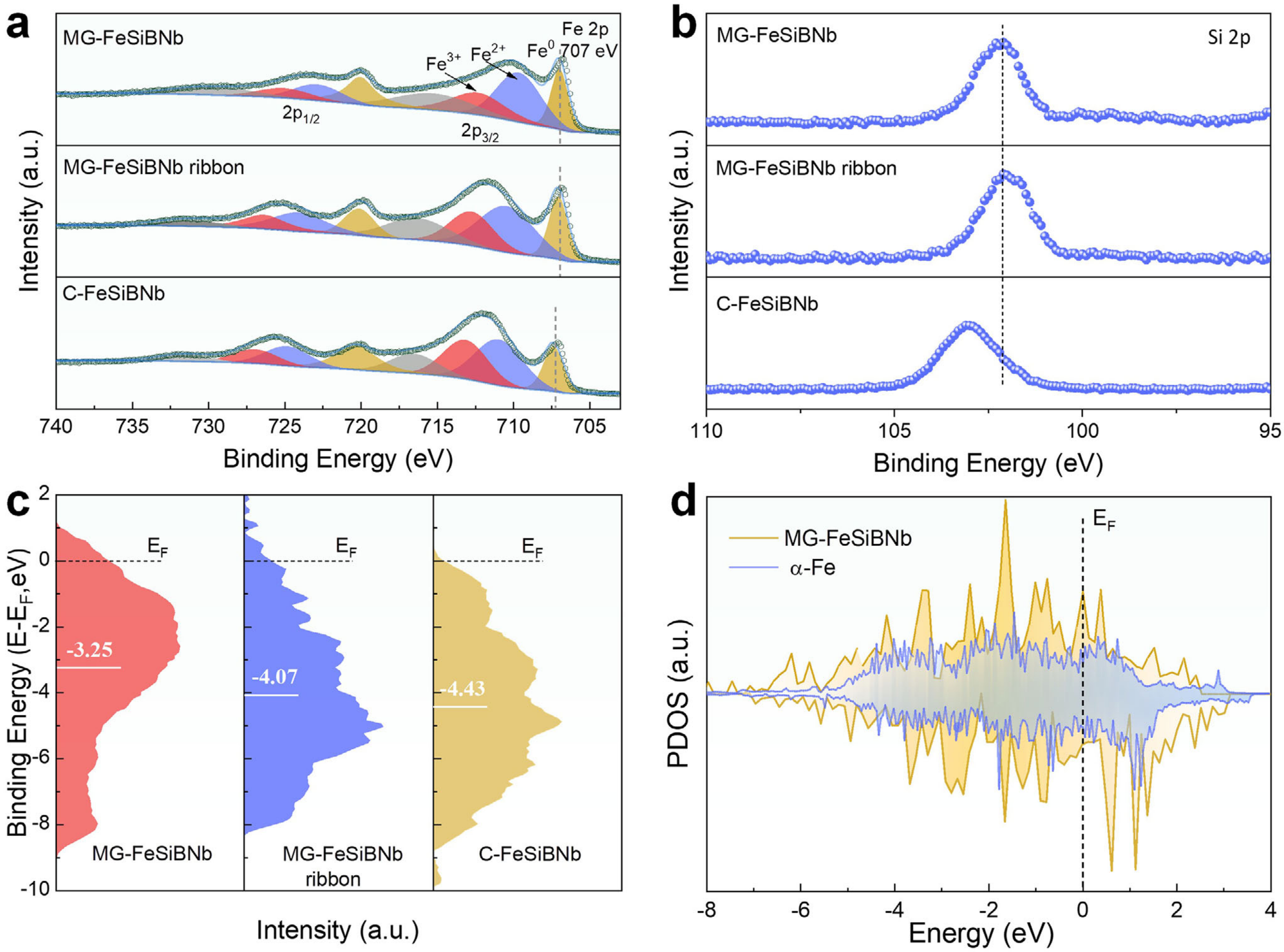

Figure 2. XPS spectra of MG-FeSiBNb, MG-FeSiBNb ribbon, and C-FeSiBNb before NRR: a) Fe 2p, b) Si 2p. c) Surface valence band photoemission spectra of MG-FeSiBNb, MG-FeSiBNb ribbon, and C-FeSiBNb. The white bars in highlight the d-band center of MG-FeSiBNb, MG-FeSiBNb ribbon, and C-FeSiBNb materials. d) The PDOS analyses for Fe d-orbital for MG-FeSiBNb and α-Fe. The Fermi energy is set at 0 eV.

Valence band XPS (VB-XPS) measurements were conducted to ascertain the adsorptive strength of the catalysts as depicted in Figure 2c (Experimental Section, Supporting Information). The d-band center of MG-FeSiBNb is positioned significantly closer to the Fermi level compared to that of MG-FeSiBNb ribbon and C-FeSiBNb, implying that the disordered phase-separated structure and the presence of additional free volumes in MG-FeSiBNb optimize its electronic structures. This structural characteristic is presumed to enhance its affinity for adsorbed substances, thereby substantially improving the NRR activity of the catalyst.

Density functional theory (DFT) calculations were conducted to further investigate the electronic environment of Fe in NRR catalysts. A simulated glassy sample of $Fe_{76}Si_8B_{13}Nb_3$, consisting of 100 atoms, was generated using a melting-quenching method via ab initio molecular dynamics (MD) simulations. Due to the multicomponent nature of MG-FeSiBNb, which often yields complex crystalline products, generating a crystalline atomistic model through simulation is challenging. In contrast, C-FeSiBNb displays a distinct α-Fe (110) peak at 44.6° (Figure S1, Supporting Information), making it a suitable candidate for analyzing the electronic structure and reaction free energy diagram. Detailed methodologies for constructing the atomistic models of MG-FeSiBNb and α-Fe are provided in the Supporting Information. To elucidate the electronic structure of the NRR catalysts, projected density of states (PDOS) analysis was performed, with a particular focus on the Fe d-orbitals (Figure 2d). Notably, the PDOS profile at the Fermi level for the adsorption site in MG-FeSiBNb reveals an enhanced electron distribution compared to crystalline α-Fe, aligning with the XPS results (Figure 2a). This suggests a higher electronic state availability in the amorphous system, which is expected to facilitate more efficient charge transfer to the reactants during the NRR process. Beyond Fe, the p-orbitals of Si and B, as well as the d-orbitals of Nb, contribute substantially to the states near the Fermi level (Figure S7, Supporting Information). Importantly, Figure S7d (Supporting Information) provides clear evidence of strong p-d orbital hybridization among Nb d, Si p, and B p states. This orbital hybridization modifies the electronic density of states in the vicinity of the Fermi level and effectively tunes the local electronic environment of the Fe active sites. Such modulation of the electronic structure enhances the electron-donating capability of the Fe active centers, thereby promoting efficient electron transfer during NRR. The increased

© 2025 Wiley-VCH GmbH

PDOS near the Fermi level is thus directly correlated with the improved catalytic activity observed in MG-FeSiBNb, highlighting the synergistic effect of multi-elemental coordination and orbital interactions in amorphous high-entropy alloys.

2.2. Electrochemical Properties of NRR

Electrochemical NRR measurements were performed under ambient conditions using an H-type electrolytic cell with a 0.1 m Na_2SO_4 electrolyte, divided into two compartments by a Nafion membrane. To ensure purity, high-purity N_2 gas was further purified using 0.05 m H_2SO_4 and 0.1 m KOH solutions to eliminate any potential NH_3 and NO_x impurities. The absence of NO_x contaminants in the N_2 gas was carefully confirmed using ultraviolet–visible (UV–vis) spectrophotometry (Figure S8, Supporting Information). The purified N_2 was then continuously fed into the cathode chamber at a flow rate of 30 sccm, ensuring that the Na_2SO_4 electrolyte was saturated with N_2 before each test. The samples used for electrochemical measurements were pre-treated with 10% HF solution for 30 s to remove any surface oxide layers prior to NRR testing. Linear sweep voltammetry (LSV) measurements for MG-FeSiBNb were performed in both Ar- and N_2-saturated 0.1 m Na_2SO_4 solutions. Distinctly, the current density of MG-FeSiBNb in the N_2-saturated electrolyte is prominently higher than that in the Ar-saturated electrolyte, indicating that MG-FeSiBNb presents observable NH_3 production activity as shown in **Figure** 3a.

The NRR activity of MG-FeSiBNb was further evaluated by chronoamperometry tests at various operating potentials (Figure 3b). After 2 h of testing, the concentrations of NH_3 and N_2H_4 produced were determined using the indole blue and Watt and Chris methods, respectively (Figures S9–S11, Supporting Information). The corresponding UV–vis absorption spectra demonstrate that MG-FeSiBNb maintains stable electrocatalytic behaviors across different operating potentials, achieving the highest absorbance at −0.8 V versus RHE as shown in Figure 3c. Remarkably, MG-FeSiBNb achieves an unprecedented NH_3 yield of 92.1 μg h^{-1} $mg^{-1}{}_{cat.}$ at −0.8 V (Figure 3d), outperforming most existing Fe-based catalysts (Figure 3e) and other NRR catalysts (Table S2, Supporting Information). This performance highlights the potential of Fe-based MGs as cutting-edge, noble-metal-free NRR catalysts. Additionally, the absence of N_2H_4 by-products after NRR electrolysis demonstrates the extraordinary NRR selectivity of MG-FeSiBNb (Figure S12, Supporting Information). Furthermore, MG-FeSiBNb also exhibits good catalytic activity (NH_3 yield rate: 59.6 μg h^{-1} $mg^{-1}{}_{cat.}$; Figure S13, Supporting Information) in 0.1 m KOH solution, indicating the wide applicability of MG-FeSiBNb. In order to directly examine the role of Fe oxidation state in catalytic activity, we performed a control experiment comparing NRR performance before and after HF treatment (Figure S14, Supporting Information). The HF-treated MG-FeSiBNb sample exhibited a significantly higher Faradaic efficiency (FE) than the untreated sample, strongly indicating that the metallic state of Fe is the active species responsible for NRR catalysis in the FeSiBNb system.

The electrocatalytic NRR performances of $Fe_{76}Si_8B_{13}Nb_3$ with different atomic configurations were evaluated under identical experimental conditions. As shown in Figure S15a (Supporting Information), the current densities of C-FeSiBNb remain relatively stable throughout 2 h of electrolysis across various applied potentials. Correspondingly, the UV–vis absorbance of the reaction solution (Figure S15b, Supporting Information) reaches its maximum at −0.8 V versus RHE, yielding an NH_3 production rate of only 14.6 μg h^{-1} $mg^{-1}{}_{cat.}$ (Figure 3d). Additionally, the absence of N_2H_4 by-products after NRR electrolysis suggests that C-FeSiBNb also exhibits good selectivity for NRR (Figure S16, Supporting Information). In addition, annealing the MG-FeSiBNb catalyst at 300 °C for 1 h (hereafter referred to as FeSiBNb-300 °C) exhibits lower catalytic performance compared to the MG-FeSiBNb (Figure S17, Supporting Information). These findings confirm that the pristine MG-FeSiBNb already possesses the optimal atomic configuration and defect sites for NRR, and that crystallization or annealing at lower temperatures offers no additional catalytic advantage. Despite sharing the same composition and glassy structure as MG-FeSiBNb, the MG-FeSiBNb ribbon achieves a notably lower NH_3 production rate of only 3.9 μg h^{-1} $mg^{-1}{}_{cat.}$ at −0.6 V versus RHE (Figure 3d; Figure S18, Supporting Information). This difference can be attributed to variations in specific surface areas; the MG-FeSiBNb ribbon, with a thickness of 10 μm, has a specific surface area approximately one-fifth that of the 2 μm thick films of MG- and C-FeSiBNb. However, even after accounting for these differences, the NH_3 production rate of the MG-FeSiBNb ribbon remains significantly lower than that of MG-FeSiBNb. This discrepancy is likely due to the intrinsic phase-separated glassy structure of MG-FeSiBNb, which modifies the electronic structure and enhances the electron density closer to the Fermi level (Figure 2c). Such structural and electronic configurations are expected to improve the adsorption affinity for reactants, thereby significantly enhancing NRR activity. These findings indicate that while MG-FeSiBNb, C-FeSiBNb, FeSiBNb-300 °C, and MG-FeSiBNb ribbon catalysts all demonstrate excellent catalytic selectively, the MG-FeSiBNb with its intrinsic phase-separated glassy structure, exhibits the highest NH_3 yield rate compared to its ribbon and crystalline counterparts. Meanwhile, the Faraday efficiency (FE) of the H_2 production by the aforementioned catalysts was evaluated (Figure S19, Supporting Information). The results show that the MG-FeSiBNb catalyst exhibits the lowest FE for H_2, suggesting its superior ability to suppress the competing HER. In addition, the electrochemical NRR performances of the α-Fe catalyst and Fe_3Si catalyst were evaluated (Figures S20 and S21, Supporting Information), both of which demonstrated poor NRR activity. As shown in Figure S22 (Supporting Information), the ammonia yield of MG-FeSiBNb is ≈6.26 times higher than that of α-Fe under identical conditions, confirming that the incorporation of Si significantly enhances NRR catalytic performance.

To conclusively verify that the detected NH_3 is directly produced by the NRR reaction catalyzed by MG- and C-FeSiBNb, systematic comparison experiments were conducted, including employing bare carbon paper (CP) as the working electrode, introducing N_2 gas into the open-circuit electrochemical reaction cell, and using Ar as the reaction gas. The resulting UV–vis absorption spectra reveal that barely trace amounts of NH_3 are detected under these control conditions (Figure S23, Supporting Information), substantiating that the observed NH_3 production and the corresponding FE are indeed a consequence of the NRR

© 2025 Wiley-VCH GmbH
16163028, 0, Downloaded from https://advanced.onlinelibrary.wiley.com/doi/10.1002/adfm.202503400 by Institute Of Physics Chinese Academy Of Sciences, Wiley Online Library on [12/08/2025]. See the Terms and Conditions (https://onlinelibrary.wiley.com/terms-and-conditions) on Wiley Online Library for rules of use; OA articles are governed by the applicable Creative Commons License

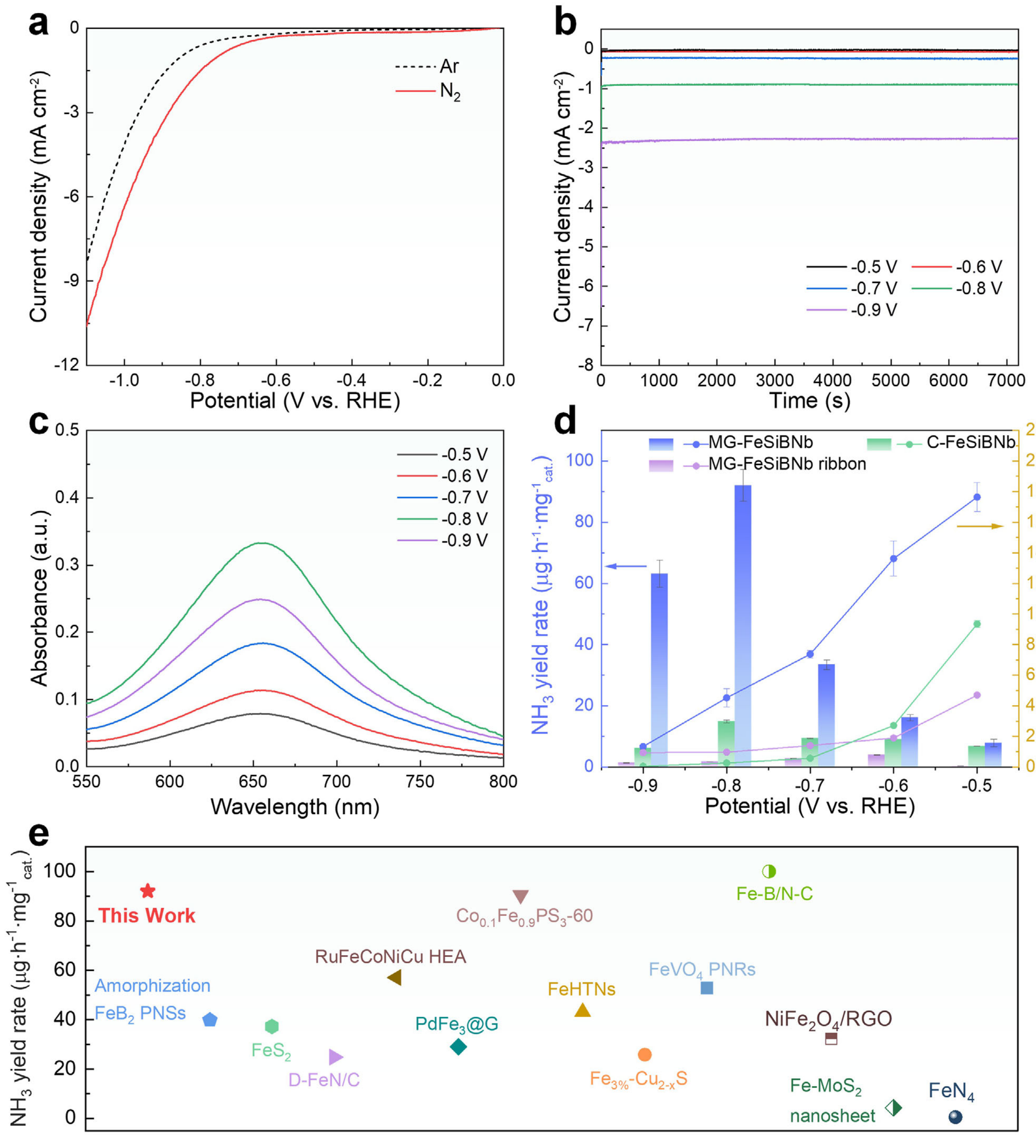

Figure 3. a) LSV curve of MG-FeSiBNb in Ar-saturated and N_2-saturated 0.1 M Na_2SO_4. b) Current densities of MG-FeSiBNb at five given voltages. c) UV–vis spectra estimated with the indophenol blue method at five given voltages. d) NH_3 yield rates and FEs for MG-FeSiBNb, C-FeSiBNb, and MG-FeSiBNb ribbon at five given voltages. e) Comparison of NH_3 yield rate of MG-FeSiBNb catalyst with other recently reported Fe-based catalysts.

facilitated by the MG- and C-FeSiBNb catalysts. In addition, to verify the nitrogen source in the produced ammonia, isotope-labeling experiments were conducted using the $^{15}N_2$ as the feeding gas and analyzed by ^1H nuclear magnetic resonance (^1H NMR) spectroscopy. As shown in Figure S24 (Supporting Information), the ^1H NMR spectra reveal two peaks corresponding to $^{15}NH_4^+$ in the electrolyte when $^{15}N_2$ was used to initiate the NRR. The above results clearly confirm that the produced NH_3 originates from the electroreduction of the feeding N_2 gas.

The stability and durability of catalysts are critical factors to evaluate the performance of electrochemical NH_3 synthesis. Accordingly, chronoamperometry tests present a steady current density over 35 h of continuous NRR for both MG- and C-FeSiBNb catalysts (**Figure** 4a; Figure S25, Supporting

© 2025 Wiley-VCH GmbH

16163028, 0, Downloaded from https://advanced.onlinelibrary.wiley.com/doi/10.1002/adfm.202503400 by Institute Of Physics Chinese Academy Of Sciences, Wiley Online Library on [12/08/2025]. See the Terms and Conditions (https://onlinelibrary.wiley.com/terms-and-conditions) on Wiley Online Library for rules of use; OA articles are governed by the applicable Creative Commons License

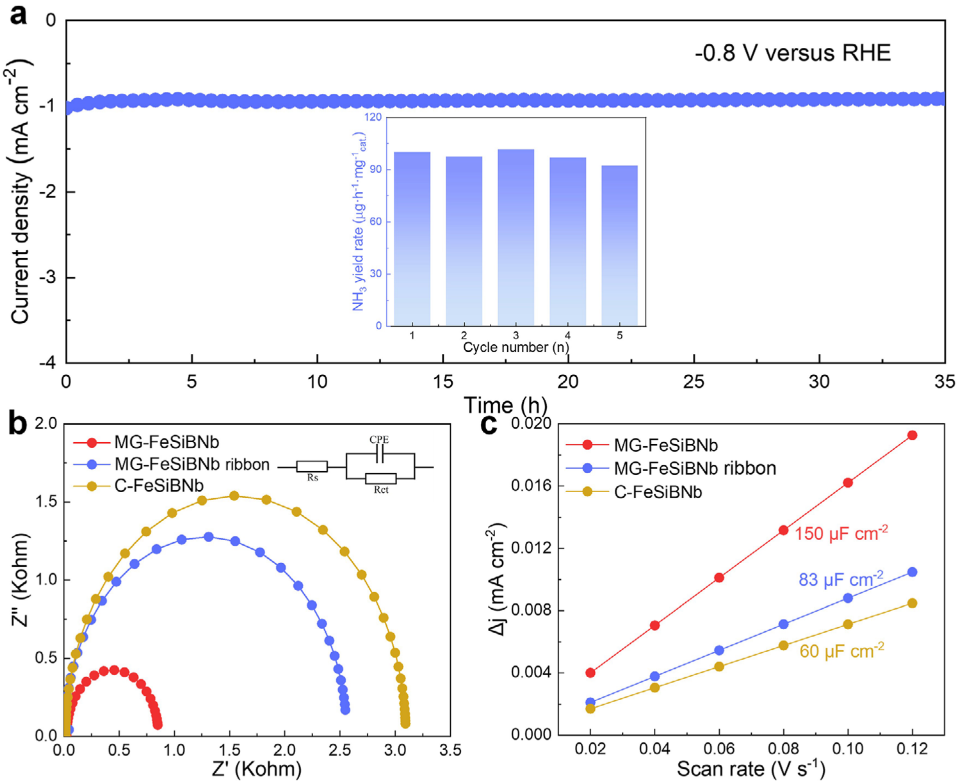

Figure 4. a) Stability tests of MG-FeSiBNb at −0.8 V for 35 h. b) EIS measurements for MG-FeSiBNb, MG-FeSiBNb ribbon, and C-FeSiBNb catalysts. c) Electrochemical double-layer capacitance (C_{dl}) of MG-FeSiBNb, MG-FeSiBNb ribbon, and C-FeSiBNb.

Information). Notably, no significant reductions in ammonia yields or FE are observed during five consecutive NRR cycles for MG-FeSiBNb (Figure 4a; Figure S26, Supporting Information). Subsequently, the MG- and C-FeSiBNb samples after stability tests were examined by powder X-ray diffraction (XRD), which confirmed the retention of their original amorphous and crystalline phases, respectively (Figure S27, Supporting Information). Scanning electron microscopy (SEM) images (Figure S28, Supporting Information) further demonstrate that both catalysts retain their original morphologies after long-term electrolysis. Moreover, XPS spectra (Figures S29 and S30, Supporting Information) of Si, B, and Nb remain largely unchanged, consistent with the pre-electrolysis state. The inductively coupled plasma analyses also show negligible variation before and after the stability test (Table S3, Supporting Information). Collectively, these results validate the structural integrity, chemical stability, and long-term viability of MG-FeSiBNb as a robust catalyst for electrochemical NH_3 production.

Electrochemical impedance spectroscopy (EIS) measurements reveal that the MG-FeSiBNb catalyst exhibits reduced charge transfer resistance, which suggests enhanced interfacial charge transfer characteristics (Figure 4b). This advantageous characteristic is primarily due to the presence of dangling bonds and improved electron distribution at the Fermi level (Figure 2d) within the amorphous structure of the material, which could facilitate electron transfer and contribute to NRR activity. To further explore the factors enhancing electrocatalytic NH_3 synthesis, electrochemical double-layer capacitance (C_{dl}) tests were conducted (Figure 4c; Figure S31, Supporting Information). The C_{dl} of the MG-FeSiBNb catalyst is measured to be 150 μF cm^{-2}, which is significantly higher than that of the MG-FeSiBNb ribbon (83 μF cm^{-2}) and C-FeSiBNb (60 μF cm^{-2}), indicating a larger electrochemically active surface area. This significant increase in active surface area can be attributed to the abundance of unsaturated coordination sites and dangling bonds in MG-FeSiBNb, which generates a proliferation of active sites, underscoring the pivotal role of amorphous material characteristics in optimizing catalytic efficiency.

2.3. Mechanism Insight

To further elucidate the reaction pathway of nitrogen conversion to ammonia on the MG-FeSiBNb catalyst, in situ infrared (IR) spectroscopic measurements were conducted (Figure S32, Supporting Information). The absorption peak at 1632 cm^{-1} is attributed to chemisorbed N_2, indicating that the catalyst has strong adsorption ability for dissolved N_2.[54] Characteristic bands at ≈3500 cm^{-1} (N–H stretching), 2916 cm^{-1}, and 1308 cm^{-1} (N–H bending, -NH_2 vibration) indicate the formation of N-containing hydrogenated intermediates, which are commonly observed during NRR. Notably, O–H stretching vibrations from interfacial water, typically absent at open circuit potential (OCP), emerge prominently at ≈303 cm^{-1} under applied potentials ranging from −0.3 to −1.2 V, with increasing intensity at more negative potentials. This behavior reflects enhanced HER activity at higher

© 2025 Wiley-VCH GmbH

16163028, 0, Downloaded from https://advanced.onlinelibrary.wiley.com/doi/10.1002/adfm.202503400 by Institute Of Physics Chinese Academy Of Sciences, Wiley Online Library on [12/08/2025]. See the Terms and Conditions (https://onlinelibrary.wiley.com/terms-and-conditions) on Wiley Online Library for rules of use; OA articles are governed by the applicable Creative Commons License

16163028, 0, Downloaded from https://advanced.onlinelibrary.wiley.com/doi/10.1002/adfm.202503400 by Institute Of Physics Chinese Academy Of Sciences, Wiley Online Library on [12/08/2025]. See the Terms and Conditions (https://onlinelibrary.wiley.com/terms-and-conditions) on Wiley Online Library for rules of use; OA articles are governed by the applicable Creative Commons License

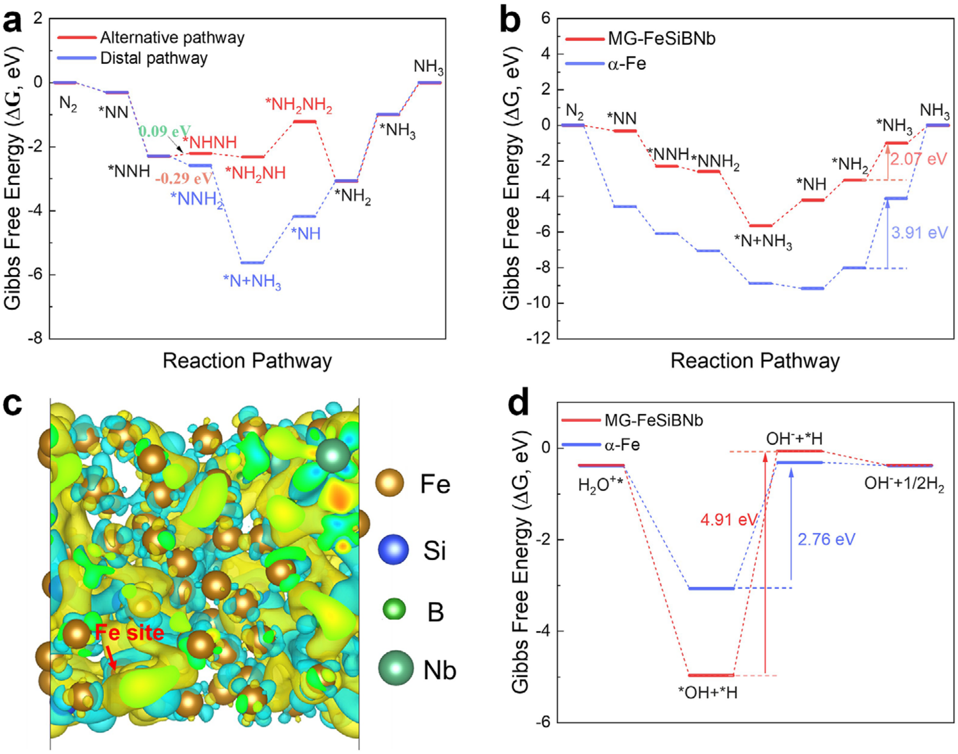

Figure 5. The asterisk (*) represents an adsorption site. a) Free energy diagram illustrating the association distal end and alternative pathway for NH_3 production in the electrocatalytic reduction reaction of MG-FeSiBNb. b) Free energy diagram of MG-FeSiBNb and *α*-Fe in the electrocatalytic NRR distal pathway. c) Gibbs free energy diagram of the HER for MG-FeSiBNb and *α*-Fe. d) Electron density difference stereograms for MG-FeSiBNb, where yellow and blue represent the charge accumulation and depletion, respectively. The brown, blue, green, and cyan spheres denote Fe, Si, B, and Nb atoms, respectively. The red five-pointed star marks the location of Fe7 site.

overpotentials. Additionally, a broad absorption band at 2078 cm^{-1}, assigned to adsorbed H atoms, further confirms the occurrence of competing HER behavior.[55] Importantly, the appearance of a distinct peak at 1423 cm^{-1}, assigned to NH_4^+, provides direct evidence for the electrochemical formation of ammonia. These in situ IR observations collectively demonstrate that the MG-FeSiBNb catalyst facilitates effective N_2 adsorption, sequential hydrogenation, and subsequent NH_3 formation. The detection of $–NH_2$ and NH_4^+ intermediates supports an associative distal pathway as the most plausible NRR mechanism on this amorphous-phase-separated catalytic surface.

To further elucidate the underlying mechanism of NRR on MG-FeSiBNb, the atomic-scale mechanisms underpinning the electrocatalytic production of NH_3 using MG-FeSiBNb were investigated through DFT calculations, with iron atoms serving as active sites (see Experimental Section for details, Supporting Information).[56] The theoretical model for MG-FeSiBNb includes seven distinct Fe sites, and both distal and alternate pathways were calculated for these sites. (**Figure 5a**; Figures S33 and S34, Supporting Information). Notably, the Fe7 site demonstrates the lowest free energy barrier (2.07 eV) for the rate-determining step (RDS), indicating its preferential role in the NRR process. Therefore, the potential reaction mechanism for NH_3 synthesis was calculated using Fe7 as the active site. The charge density differences for N_2 adsorbed on MG-FeSiBNb and *α*-Fe materials were obtained by DFT calculation. As illustrated in Figure S35 (Supporting Information), the N_2 molecule adsorbed on MG-FeSiBNb exhibits a greater electron gain (0.58 e^-) compared to that on *α*-Fe (0.56 e^-), which indicates a stronger electronic interaction between N_2 and the Fe active site within the amorphous matrix. This enhanced charge transfer suggests that the incorporation of Si, B, and Nb into the MG-FeSiBNb modulates the local electronic environment, thereby improving the N_2 activation capability of the catalyst. To elucidate the specific reaction pathway facilitated by MG-FeSiBNb, both distal and alternate pathways were simulated via DFT calculations (Figure 5a). In the reaction process from $^*NNH$ to $^*NNH_2$, the distal pathway exhibits a negative Gibbs free energy barrier (−0.29 eV) compared to the alternate pathway, indicating the distal pathway as the preferred mechanism for NH_3 production in the NRR process of MG-FeSiBNb. Notably, this mechanistic preference is consistent with the in situ IR spectroscopic observations (Figure S32, Supporting Information), further supporting the proposed reaction pathway. Furthermore, a comparative analysis of the free energy barrier of the distal pathway for both MG-FeSiBNb and *α*-Fe catalysts reveals that the $^*NH_2 \rightarrow {}^*NH_3$ step plays a crucial role in determining the NRR reaction rate (Figure 5b). Notably, MG-FeSiBNb shows a significantly lower free energy barrier for this step (2.07 eV) compared to *α*-Fe (3.91 eV). This substantial difference is attributed to the unique unsaturated coordination and defect sites inherent in the amorphous structure of MG-FeSiBNb, which effectively reduce the free energy barrier of the

© 2025 Wiley-VCH GmbH

NRR process. Charge density distribution analysis (Figure 5c) further demonstrates that Si atoms in MG-FeSiBNb modulate the electronic environment surrounding Fe atoms in the amorphous state, facilitating efficient electron transfer between Fe and Si atoms. This leads to an increased number of unpaired d-orbital electrons in Fe, consequently facilitating the hydrogenation step from $^*NH_2$ to $^*NH_3$, which is highly beneficial for electrocatalytic NRR reactions.

As a competitive process, the hydrogen evolution reaction (HER) possesses a standard potential similar to that of NRR but exhibits considerably faster reaction kinetics. Consequently, most catalysts inherently favor HER over NRR, leading to reduced NH_3 selectivity. The adsorption energy of H atoms was analyzed to evaluate catalyst selectivity during NRR (Figure 5d). For crystalline α-Fe, the HER process is energetically more favorable than the NRR, with a lower energy barrier of 2.76 eV (Figure 5b,d). In contrast, MG-FeSiBNb exhibits a significantly higher HER barrier of 4.91 eV (Figure 5d). These simulation results suggest that MG-FeSiBNb not only enhances NRR activity but also effectively suppresses the HER process (Figure 3d), which is consistent with the above H_2 FE results. Consequently, its structural characteristics promote more efficient electrocatalytic NH_3 synthesis.

3. Conclusion

In conclusion, a noble-metal-free MG-FeSiBNb catalyst featuring intrinsic nanoscale phase separation is achieved via a straightforward deposition approach, which demonstrates an exceptionally high NH_3 yield rate of 92.1 $\mu g\ h^{-1}\ mg^{-1}_{cat.}$ at −0.8 V versus RHE. The incorporation of Si, B, and Nb into the Fe-based matrix precisely tailors the local electronic environment, leading to a shift of the Fe d-band center toward the Fermi level, enhancing electron transfer efficiency and facilitating the hydrogenation of $^*NH_2$ to $^*NH_3$. Additionally, the inherent amorphous structure of MG-FeSiBNb suppresses hydrogen adsorption by eliminating clearly defined crystalline facets, selectively minimizing the competing HER and thus notably enhancing NRR selectivity. The MG-FeSiBNb catalyst demonstrates robust cycling and long-term stability, maintaining consistent current density over 35 h of continuous NRR operation. This work illustrates a simple yet effective strategy for developing highly efficient NRR catalysts by leveraging the advantages of an amorphous material framework to modulate the electron environment and optimize catalytic activity.

4. Experimental Section

Catalyst Synthesis: $Fe_{76}Si_8B_{13}Nb_3$ ingot using arc-melting high-purity Fe, Si, B, and Nb (purity ≥ 99.99%) under a high-purity argon atmosphere. The ingot was re-melted five times to ensure compositional homogeneity. Subsequently, amorphous $Fe_{76}Si_8B_{13}Nb_3$ ribbons were fabricated using a melt-spinning technique under argon protection. The alloy ingot was remelted via induction heating, and the molten alloy was ejected through a nozzle onto a rapidly rotating copper wheel with a linear surface velocity of 43.9 $m\ s^{-1}$. This rapid quenching process produced metallic glass ribbons with a thickness of ≈10 µm and a width of 2 mm. $Fe_{76}Si_8B_{13}Nb_3$ MG films were fabricated by ion beam deposition (IBD) on a flat polymethyl methacrylate (PMMA) plate. Specifically, the deposition was carried out using a pre-alloyed $Fe_{76}Si_8B_{13}Nb_3$ target (atomic ratio). The base pressure before deposition was better than 4.0×10^{-4} Pa, and the deposition environmental pressure was maintained at 2.6×10^{-2} Pa by a high-purity argon supplement. An ion beam with an energy of 750 eV bombarded the target, and the sputtered atoms were deposited on the substrate with a thickness of 2 µm. The films were immersed in alcohol for 10 min to peel from the PMMA substrate (alcohol reduces the van der Waals force between the film and the substrate),[57] then the film was lightly treated with a 10% HF solution for 30 s to remove any potential oxidation layer. The corresponding crystallized counterpart (C-FeSiBNb) was achieved by annealing as-deposited films at 900 °C for 1 h in a high vacuum tube furnace with a base pressure better than 1.0×10^{-4} Pa. The as-deposited (MG-FeSiBNb) and C-FeSiBNb films were treated with ultrasonication for 5 min in alcohol, resulting in a fragmentary size of ≈50 µm. The $Fe_{76}Si_8B_{13}Nb_3$ MG ribbons with a thickness of 10 µm and a width of 2 mm were prepared by melt-spinning under argon atmosphere. The transmission electron microscopy specimens were prepared by ion milling (Gatan, PIPS II 695) at 3 kV and were finally polished with low-voltage (0.5 kV) with a liquid-nitrogen-cooled stage.

Electrochemical Measurement: All electrochemical characterizations were conducted using a CHI760E electrochemical workstation by a two-chamber H-type electrolytic cell separated by a Nafion 117 membrane in 0.1 м Na_2SO_4 solution. The working electrode, counter electrode, reference electrode, the catalyst-modified carbon cloth, platinum net, and saturated Ag/AgCl were employed, respectively. The Nafion membrane was treated as follows: it was initially boiled in deionized water for 1 h, separately treated in H_2O_2 (5 wt.%) aqueous solution at 80 °C for 3 h. Then, the membrane was trampled in 0.5 м H_2SO_4 at 80 °C for 2 h. The membrane was finally treated in 0.5 м H_2SO_4 for 4 h at 100 °C. The measured potential ($E_{Ag/AgCl}$) was converted to the reversible hydrogen electrode potential (E_{RHE}) according to the following equation:

$$E_{RHE} = 0.197\ V + 0.059 \times pH + E_{Ag/AgCl} \tag{1}$$

Prior to measurements, the solution was purified through high-purity nitrogen gas for at least 30 min. The measured current density was normalized to the geometric surface area. Chronoamperometry curves were obtained in a N_2-saturated 0.1 м Na_2SO_4 solution after a 30 min N_2 purge at room temperature as part of the electrocatalytic nitrogen fixation experiment.

Supporting Information

Supporting Information is available from the Wiley Online Library or from the author.

Acknowledgements

X.C. and X.P. contributed equally to this work. This work was supported by the National Key R&D Program of China (Grant No. 2021YFB3802900), the National Natural Science Foundation of China (Grant Nos. 52192601, 52192604, 52371166, and 62104131), the Higher Educational Youth Innovation Science and Technology Program Shandong Province (2021KJ022), Taishan Scholars Program (tsqn201909107), Natural Science Foundation of Shandong Province (ZR2020QF077). This work was supported by the Center for Materials Genome and the Synergetic Extreme Condition User Facility (SECUF).

Conflict of Interest

The authors declare no conflict of interest.

Data Availability Statement

The data that support the findings of this study are available from the corresponding author upon reasonable request.

© 2025 Wiley-VCH GmbH

16163028, 0, Downloaded from https://advanced.onlinelibrary.wiley.com/doi/10.1002/adfm.202503400 by Institute Of Physics Chinese Academy Of Sciences, Wiley Online Library on [12/08/2025]. See the Terms and Conditions (https://onlinelibrary.wiley.com/terms-and-conditions) on Wiley Online Library for rules of use; OA articles are governed by the applicable Creative Commons License

Keywords

d-band center, metallic glasses, nitrogen reduction reaction, unsaturated coordination

Received: May 16, 2025
Revised: July 17, 2025
Published online:

---

[1] J. G. Chen, R. M. Crooks, L. C. Seefeldt, K. L. Bren, R. M. Bullock, M. Y. Darensbourg, P. L. Holland, B. Hoffman, M. J. Janik, A. K. Jones, *Science* **2018**, *360*, aar6611.

[2] D. Chen, M. Luo, S. Ning, J. Lan, W. Peng, Y. R. Lu, T. S. Chan, Y. Tan, *Small* **2022**, *18*, 2104043.

[3] M. Jiang, J. Su, X. Song, P. Zhang, M. Zhu, L. Qin, Z. Tie, J.-L. Zuo, Z. Jin, *Nano Lett.* **2022**, *22*, 2529.

[4] S. Z. Andersen, V. Čolić, S. Yang, J. A. Schwalbe, A. C. Nielander, J. M. McEnaney, K. Enemark-Rasmussen, J. G. Baker, A. R. Singh, B. A. Rohr, *Nature* **2019**, *570*, 504.

[5] J. N. Galloway, A. R. Townsend, J. W. Erisman, M. Bekunda, Z. Cai, J. R. Freney, L. A. Martinelli, S. P. Seitzinger, M. A. Sutton, *Science* **2008**, *320*, 889.

[6] J. Zhao, A. S. Goldman, J. F. Hartwig, *Science* **2005**, *307*, 1080.

[7] M. Jiang, L. Han, P. Peng, Y. Hu, Y. Xiong, C. Mi, Z. Tie, Z. Xiang, Z. Jin, *Nano Lett.* **2021**, *22*, 372.

[8] X. Xue, R. Chen, C. Yan, P. Zhao, Y. Hu, W. Zhang, S. Yang, Z. Jin, *Nano Res.* **2019**, *12*, 1229.

[9] Q. Li, Z. Xiao, W. Jia, Q. Li, X. Li, W. Wang, *Nano Res.* **2023**, *16*, 12357.

[10] L. Gao, C. Guo, M. Zhao, H. Yang, X. Ma, C. Liu, X. Liu, X. Sun, Q. Wei, *ACS Appl. Mater. Interfaces* **2021**, *13*, 50027.

[11] T. Wu, H. Zhao, X. Zhu, Z. Xing, Q. Liu, T. Liu, S. Gao, S. Lu, G. Chen, A. M. Asiri, *Adv. Mater.* **2020**, *32*, 2000299.

[12] L. Li, C. Tang, H. Jin, K. Davey, S.-Z. Qiao, *Chem* **2021**, *7*, 3232.

[13] J. Wang, T. Feng, J. Chen, V. Ramalingam, Z. Li, D. M. Kabtamu, J.-H. He, X. Fang, *Nano Energy* **2021**, *86*, 106088.

[14] A. U. Shetty, R. Sankannavar, *J. Energy Chem.* **2024**, *92*, 681.

[15] X. Li, X. Ren, X. Liu, J. Zhao, X. Sun, Y. Zhang, X. Kuang, T. Yan, Q. Wei, D. Wu, *J. Mater. Chem. A* **2019**, *7*, 2524.

[16] L. Zhang, L. X. Ding, G. F. Chen, X. Yang, H. Wang, *Angew. Chem.* **2019**, *131*, 2638.

[17] X. Chen, H. Yin, X. Yang, W. Zhang, D. Xiao, Z. Lu, Y. Zhang, P. Zhang, *Inorg. Chem.* **2022**, *61*, 20123.

[18] J. Zheng, Y. Lyu, M. Qiao, R. Wang, Y. Zhou, H. Li, C. Chen, Y. Li, H. Zhou, S. Wang, *Chem* **2019**, *5*, 617.

[19] X. Wang, M. Luo, J. Lan, M. Peng, Y. Tan, *Adv. Mater.* **2021**, *33*, 2007733.

[20] X. Guo, H. Du, F. Qu, J. Li, *J. Mater. Chem. A* **2019**, *7*, 3531.

[21] B. Zhang, Y. Chen, J. Wang, H. Pan, W. Sun, *Adv. Funct. Mater.* **2022**, *32*, 2202227.

[22] L. Shi, Y. Yin, S. Wang, H. Sun, *ACS Catal.* **2020**, *10*, 6870.

[23] T. Xu, J. Liang, S. Li, Z. Xu, L. Yue, T. Li, Y. Luo, Q. Liu, X. Shi, A. M. Asiri, *Small Sci.* **2021**, *1*, 2000069.

[24] D. Liu, M. Chen, X. Du, H. Ai, K. H. Lo, S. Wang, S. Chen, G. Xing, X. Wang, H. Pan, *Adv. Funct. Mater.* **2021**, *31*, 2008983.

[25] A. Biswas, S. Bhardwaj, T. Boruah, R. S. Dey, *Mater. Adv.* **2022**, *3*, 5207.

[26] Y. Li, H. Wang, C. Priest, S. Li, P. Xu, G. Wu, *Adv. Mater.* **2021**, *33*, 2000381.

[27] Y.-C. Hao, Y. Guo, L.-W. Chen, M. Shu, X.-Y. Wang, T.-A. Bu, W.-Y. Gao, N. Zhang, X. Su, X. Feng, *Nat. Catal.* **2019**, *2*, 448.

[28] X. Peng, J. Han, Y. Wang, Z. Bo, A. Nie, P. Li, Y. Li, H. Wu, P. Liu, Z. Lu, *Appl. Mater. Today* **2022**, *29*, 101689.

[29] A. L. Greer, *Science* **1995**, *267*, 1947.

[30] P. G. Debenedetti, F. H. Stillinger, *Nature* **2001**, *410*, 259.

[31] A. L. Greer, E. Ma, *MRS Bull.* **2007**, *32*, 611.

[32] L.-C. Zhang, Z. Jia, F. Lyu, S.-X. Liang, J. Lu, *Prog. Mater. Sci.* **2019**, *105*, 100576.

[33] Z. Jia, X. Duan, P. Qin, W. Zhang, W. Wang, C. Yang, H. Sun, S. Wang, L. C. Zhang, *Adv. Funct. Mater.* **2017**, *27*, 1702258.

[34] S. X. Liang, Z. Jia, Y. J. Liu, W. Zhang, W. Wang, J. Lu, L. C. Zhang, *Adv. Mater.* **2018**, *30*, 1802764.

[35] T. Zhang, M.-Y. Wu, D.-Y. Yan, J. Mao, H. Liu, W.-B. Hu, X.-W. Du, T. Ling, S.-Z. Qiao, *Nano Energy* **2018**, *43*, 103.

[36] R. Wu, J. Zhang, Y. Shi, D. Liu, B. Zhang, *J. Am. Chem. Soc.* **2015**, *137*, 6983.

[37] S. Mukherjee, R. C. Sekol, M. Carmo, E. I. Altman, A. D. Taylor, J. Schroers, *Adv. Funct. Mater.* **2013**, *23*, 2708.

[38] G. Doubek, R. C. Sekol, J. Li, W. H. Ryu, F. S. Gittleson, S. Nejati, E. Moy, C. Reid, M. Carmo, M. Linardi, *Adv. Mater.* **2016**, *28*, 1940.

[39] Y. Cheng, E. Ma, *Prog. Mater. Sci.* **2011**, *56*, 379.

[40] R. Jiang, Y. Da, Z. Chen, X. Cui, X. Han, H. Ke, Y. Liu, Y. Chen, Y. Deng, W. Hu, *Adv. Energy Mater.* **2022**, *12*, 2101092.

[41] N. Sezer, Z. Evis, S. M. Kayhan, A. Tahmasebifar, M. Koç, *J. Magnes. Alloy.* **2018**, *6*, 23.

[42] L. C. Zhang, S. X. Liang, *Chem. Asian J.* **2018**, *13*, 3575.

[43] Y.-X. Ge, P.-Y. Zhu, Y. Yu, L.-C. Zhang, C. Zhang, L. Liu, *J. Mater. Chem. A* **2022**, *10*, 23314.

[44] M. Liu, H. Su, X. Liu, X. He, P. Tan, F. Liu, J. Pan, *Nat. Commun.* **2025**, *16*, 2826.

[45] Y. Wang, S. Li, X. Hou, T. Cui, Z. Zhuang, Y. Zhao, H. Wang, W. Wei, M. Xu, Q. Fu, *Adv. Mater.* **2024**, *36*, 2412598.

[46] J. Rumble Jr, D. Bickham, C. Powell, *Surf. Inter. Anal.* **1992**, *19*, 241.

[47] Z. Zeng, X. Ma, W. Ding, W. Li, *Sci. China Chem.* **2010**, *53*, 402.

[48] Q. Dai, L. Wang, K. Wang, X. Sang, Z. Li, B. Yang, J. Chen, L. Lei, L. Dai, Y. Hou, *Adv. Funct. Mater.* **2022**, *32*, 2109556.

[49] Y. Wang, X. Lin, G. Zhang, H. Gao, Z.-J. Zhao, P. Zhang, T. Wang, J. Gong, *Proc. Natl. Acad. Sci. USA* **2023**, *120*, 2305604120.

[50] M. Yang, X. Wang, C. J. Gómez-García, Z. Jin, J. Xin, X. Cao, H. Ma, H. Pang, L. Tan, G. Yang, *Adv. Funct. Mater.* **2023**, *33*, 2214495.

[51] J. R. Kitchin, J. K. Nørskov, M. A. Barteau, J. G. Chen, *J. Chem. Phys.* **2004**, *120*, 10240.

[52] J. K. Nørskov, T. Bligaard, J. Rossmeisl, C. H. Christensen, *Nat. Chem.* **2009**, *1*, 37.

[53] H. Xin, A. Holewinski, N. Schweitzer, E. Nikolla, S. Linic, *Top. Catal.* **2012**, *55*, 376.

[54] P. Li, Z. Zhou, Q. Wang, M. Guo, S. Chen, J. Low, R. Long, W. Liu, P. Ding, Y. Wu, *J. Am. Chem. Soc.* **2020**, *142*, 12430.

[55] Y. Yao, S. Zhu, H. Wang, H. Li, M. Shao, *J. Am. Chem. Soc.* **2018**, *140*, 1496.

[56] Z. Chen, Y. Ye, T. Peng, C. Wu, H. Li, X. Pan, X. Bao, *ACS Catal.* **2023**, *13*, 14385.

[57] S.-Q. Chen, Y. Shao, M.-T. Cheng, K.-F. Yao, *J. Non Cryst. Solids* **2017**, *473*, 74.

© 2025 Wiley-VCH GmbH

16163028, 0, Downloaded from https://advanced.onlinelibrary.wiley.com/doi/10.1002/adfm.202503400 by Institute Of Physics Chinese Academy Of Sciences, Wiley Online Library on [12/08/2025]. See the Terms and Conditions (https://onlinelibrary.wiley.com/terms-and-conditions) on Wiley Online Library for rules of use; OA articles are governed by the applicable Creative Commons License